Demonstration of efficient relativistic electron acceleration by surface plasmonics with sequential target processing using high repetition lasers

Yasunobu Arikawa [1], Alessio Morace [1], Yuki Abe,[1,2] Natsumi Iwata [1,3] Yasuhiko Sentoku,[1] Akifumi Yogo [1], Kazuki Matsuo [1], Mitsuo Nakai,[1] Hideo Nagatomo,[1] Kunioki Mima,[1] Hiroaki Nishimura,[1,4] Shinsuke Fujioka [1], Ryosuke Kodama,[1] Shunsuke Inoue,[5] Masaki Hashida [5,6] Shuji Sakabe,[5] Diego De Luis [7], Giancarlo Gatti [7], Marine Huault,[7,8] José Antonio Pérez-Hernández [7], Luis Roso [7], and Luca Volpe[7]

[1]*Institute of Laser Engineering, Osaka University, 2–6, Yamadaoka, Suita, Osaka 565-0871, Japan*
[2]*Graduate School of Engineering, Osaka University, 2-1, Yamadaoka, Suita, Osaka 565-0871, Japan*
[3]*Institute for Advanced Co-Creation Studies, Osaka University, 1-1, Yamadaoka, Suita, Osaka 565-0871, Japan*
[4]*Fukui University of Technology, 2-6-1, Gakuen, Fukui City, Fukui 910-8505, Japan*
[5]*Advanced Research Center for Beam Science Institute for Chemical Research, Kyoto University, Gokasho Uji city, Kyoto 611-0011, Japan*
[6]*Research Institute of Science and Technology, Tokai University, 4-1-1 Kitakaname, Hiratsuka, Kanagawa 259–1292, Japan*
[7]*Centro de Láseres Pulsados, CLPU, Spain, Edificio M5. Calle del Adaja, 37185 Vilamayor, Salamanca, Spain*
[8]*Departamento de Física Fundamental, Universidad de Salamanca, E-37008 Salamanca, Spain*

For high repetition ultrahigh-intensity laser system, automatic alignment of structured target is key to achieving consistent particle acceleration and plasma heating. In this work, we demonstrate efficient electron acceleration with two sequential steps of laser processing using a high repetition rate, 30-fs ultrahigh-intensity laser. The first pulse does laser machining and creates a steep cylindrical crater on the surface of a flat stainless-steel target. The crater is formed by the hydrodynamic expansion of the heated surface and by spallation of the inner, deeper material by nonthermal relativistic electrons. The crater shape is well controlled and reproducible with 200 μm width and 350 μm depth. The second pulse irradiates deeply inside the crater and interacts with the crater wall, efficiently accelerating electrons via surface plasmonic, without need for target realignment. The laser absorption efficiency increases from 32.5 to 97.5% by the process.

I. INTRODUCTION

High power lasers are widely used in laser machining, given their excellent fineness and accuracy in manufacturing for various applications [1–3]. In recent years, the development of high repetition rate petawatt-class lasers sparked the development of plasma-based accelerators, with a large amount of research dedicated to ultrarelativistic electron sources via laser wake-field acceleration and more recently to the development of ion-based plasma accelerators [4–7].

Moreover, these laser systems can produce bright γ-ray and neutron sources to be utilized as radiographic tools for material structures or for nuclear isotopes production [8–13]. When an ultraintense laser strikes to a solid target with a short scale-length preformed plasma, hot electrons are mainly generated by two processes: vacuum heating, where electrons are accelerated normally to the plasma density gradient by the normal component of the laser electric field [14], and $j \times B$ heating, where electrons are accelerated by the high frequency term of the ponderomotive force [15]. Electron energies for these mechanisms are limited to a few MeV and a great deal of effort by the scientific community has been focused onto improving the hot electron energy output in laser-solid interaction. Amongst the various approaches, the usage of micro- and nanostructured targets was thoroughly investigated and provided some promising results [16–21]. Despite the clear advantages demonstrated by these techniques, a major drawback are the constraints of single-shot operation as opposed to high repetition rate, alignment accuracy, and manufacturing costs for these types of targets.

In this work we demonstrate that *in situ* laser machining allows to greatly enhance the laser-energy absorption into hot electrons while allowing for high repetition rate laser operation, thus opening the door to direct application of bright laser-generated radiation sources.

For electron acceleration, accurate reproducibility of energy and current density of electron beams in a high repetition rate laser system is essential for applications. Intense laser focused onto a flat target, such as a tape foil or a flat rotating disk target, accelerates electrons in a preformed plasma mainly via ponderomotive force as described by Wilks *et al.* [22]. For an ultrahigh contrast laser ($\sim 10^{10}$) focused near the normal to the target surface, the electron acceleration becomes inefficient due to a sharp density profile at the interaction surface. Therefore, the electron mean energy T_e is reduced compared to the ponderomotive scaling as discussed by Chrisman *et al.*

(a) Flat target

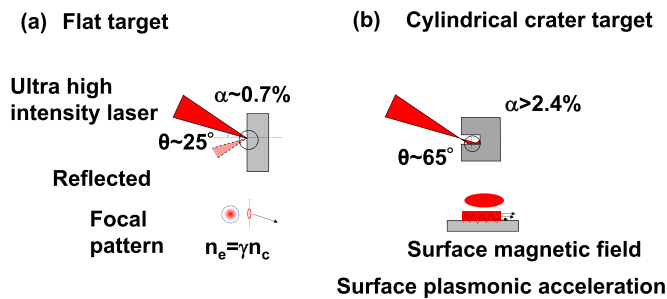**(b) Cylindrical crater target**

FIG. 1. Schematic comparison between simple flat target (a) and cylinder crater target with surface plasmonic acceleration (b).

[23]:

$$T_e = m_e c^2 (\gamma - 1) \sqrt{\frac{\gamma n_c}{n_s}}, \tag{1}$$

where m_e is the electron mass, c is speed of light, γ is Lorenz factor given in terms of laser intensity $I(\text{W/cm}^2)$

$$\gamma = \sqrt{1 + \frac{I\lambda^2}{1.37 \times 10^{18}}}, \tag{2}$$

λ is the laser wavelength in micrometers, n_c is the critical density for the 0.8-μm laser (1.75×10^{21} cm^{-3}), and n_s is the electron density of the solid stainless steel. The scale length L of the "sharp" plasma density gradient at the laser-irradiated surface is defined experimentally as $L \lesssim \frac{c}{\omega_p}$, where ω_p is plasma frequency, $\omega_p^2 = 4\pi n_e e^2 / m_e$, then $L \lesssim 4 \, \mu$m [24]. In our experimental conditions we can consider the preplasma-scale length to be $L = 0.5 \, \mu$m, and the solid density of the stainless steel is $n_s = 1.5 \times 10^{23}$ cm^{-3}. For an ultrahigh contrast Ti:sapphire laser with intensity $I = 10^{20}$ W/cm^2 and $\lambda = 0.8 \, \mu$m, interacting at near-solid density [see Fig. 1(a)], the resulting hot electron temperature T_e is 0.9 MeV as given by Eq. (1) and the maximum electron energy $E_{\max} = 15$ MeV, the latter obtained by using the equation for free-acceleration limit $E_{\max} = a_0^2 m_e c^2 / 2$ [25].

The total number of accelerated electrons is estimated as

$$N_{\text{total}} = S v_e \tau \gamma n_c \cong S c \tau \gamma n_c, \tag{3}$$

where S is the focal spot area of the laser, v_e is the average electron velocity, and τ is pulse duration of the laser. The last form is obtained by replacing the electron velocity with the speed of light c. Since the energy of relativistic intensity lasers is absorbed at relativistic critical density plasma density γn_c within the volume $S c \tau$, the total number of accelerated is calculated in first approximation as $S c \tau \times g n_c$. Here we are considering S as the experimentally observed laser spot size which corresponds approximately to a 2D Gaussian intensity distribution containing 20% of the laser energy within the full width at half maximum. For the current experiment, in case of flat target we had $S = 3.8 \times 10^{-7}$ cm^2 and N_{total} becomes 4.6×10^{10}. The total electron energy is given by αE_{laser} where α is the laser-to-electron energy conversion efficiency and E_{laser} is the laser energy. From the energy conservation the following condition must be satisfied:

$$\alpha E_{\text{laser}} \approx N_{\text{total}} T_e. \tag{4}$$

The absorbed laser energy is greater than the total electron energy since a part of the energy will be transferred to the ions and electromagnetic fields. α is about 0.8% for the case with $I = 10^{20}$ W/cm^2, $\lambda = 0.8 \, \mu$m. A laser having an ultrahigh contrast and nearly normal incidence angle is not efficiently absorbed and about 60% of the laser energy is unavoidably reflected. Note that E_{laser} is the laser energy contained within the focal spot (having 10^{20} W/cm^2 in average), and it does not correspond to the total laser pulse energy since the focal spot contains only 20% of the total laser energy. Since α is intensity dependent ($\sim I$) [22], the remaining 80% of light surrounding the spot will not contribute to electron acceleration.

An electron beam with 0.9-MeV temperature and total charge of 3.4 nC, which is 0.8% of the injected laser energy, does not represent a viable source for accelerator applications. Relativistic electron-beam currents greater than 1 μC/s [26] are required for the neutron generation and neutron radiography applications. Laser-based electron accelerators provide currents lower than 10 nC/s [27], which are insufficient for the purpose. Radiography techniques using electron-generated neutrons have not yet been developed, and this work represents a step in this direction, demonstrating that very high brightness electron beams can be generated with high repetition rate.

To increase T_e and N_{total}, the most immediate solution would be to increase the laser intensity I, but it would come at a large cost since it would imply laser system upgrades. Other possible methods would include increasing the acceleration time t and interaction area S. Laser wake-field acceleration [28], laser-plasma instability-driven acceleration [29] and surface plasmonic acceleration [30–33] are based on this concept. The first two approaches are based on gas-jet targets which allows for high repetition rate operation at the cost of very low number of accelerated electrons due to low gas-jet density ($ne < 0.1 \, n_c$).

In this work we propose to generate bright ultrarelativistic electron beams by surface plasmonic acceleration on the surface of a laser-processed solid target under oblique irradiation. The laser focused onto a cylindrical target inner wall with shallow incidence angle and large spot size can dramatically boost the ultrarelativistic electron-beam generation. Fig. 1 shows the schematic comparison of laser irradiation of flat target and a cylindrical laser-machined crater target where surface plasmonic acceleration occurs. For the latter case, a strong surface magnetic field and an electrostatic sheath field confine electrons on the target surface and excite the oscillating plasmonic waves. When intense, P-polarized laser pulses irradiate solid targets with short scale-length preplasma (shorter than the laser wavelength $L < 0.8 \, \mu$m), and incidence angle $>65°$, electrons are mainly accelerated by surface plasmonic generated and propagating along the target surface. The magnetic field associated with the electron current prevents the electrons from penetrating the over-dense plasma, while the charge-separation electric field confines the electrons on the target surface, therefore undergoing continuous acceleration and boosting the relativistic electron energy to values much higher than standard laser-solid interaction at shallow angle would [30].

The electrons are therefore continuously accelerated along the target surface until they move out of the laser focal

spot area. For continuous surface acceleration to occur, the Larmor radius r_L of the electrons must be smaller than the excursion length $r_{os} = a_0\lambda/2\pi$ in the laser field where $a_0 = eE_L/(m_e c\omega)$ is the normalized vector potential and E_L is the laser electric field. The maximum electron momentum $p_{\max}$ is estimated by the condition $r_L \sim r_{os}$ as $p_{\max}/m_e c = 2\pi b_s r_{os}/\lambda$, where $b_s = eB_s/(m_e c\omega)$, B_s being the surface magnetic field and ω being the laser frequency. The maximum energy an electron can gain is described as [30]

$$E_{\max} = m_e c^2 \left(\sqrt{1 + \left(\frac{p_{\max}/m_e c}{1 - \sin\theta} \right)^2} - 1 \right), \qquad (5)$$

where θ is the laser incidence angle. For values of $b_s \sim 0.5\, a_0$, $a_0 \sim 4$, and $\theta = 65°$ we obtain a maximum electron energy $E_{\max} \sim 40$ MeV. $(1 - \sin\theta)$ components which is coming from the balance between magnetic field potential and target normal component $P_{\max}\sin\theta$ indicates a larger θ can gain a larger energy from the mechanism [30]. The maximum electron energy is estimated for a given angle θ and momentum P, with normal component and parallel component being $Pz = P\cos\theta$, $P_x = P\sin\theta$, respectively. The magnetic potential $A(z)$ reflects the electron at the target surface. By momentum conservation, the maximum momentum an electron can attain is $P_{\max} \leq A(z)/1 - \sin\theta$.

The mean electron energy is estimated from the cycle-averaged electron oscillation energy in a laser electric field with shallow incident angle as $T_e = m_e c^2 (\gamma - 1) \simeq 1.1$ MeV. The process also significantly increases the total number of accelerated electrons. For defocused laser pulses such as the one we expect to interact with the crater wall, the quasitotality of laser energy is encircled in the focal spot. By geometrical considerations we can see that the laser intensity for the crater irradiation case is reduced approximately 25 times, while the encircled energy in the focal spot is increased by 5 times. In defocused conditions the energy in the (larger) focal spot is approximately 100% of the laser energy. Therefore, applying again Eq. (3), N_{total} becomes 5.4×10^{11} (86 nC), which is increased by 25 times compared to the flat target. Then α becomes greater than 2.4% because there are nonthermal hot electron components ($T > T_e$). This value is one of the highest values in high repetition late electron acceleration by relativistic intensity lasers. Moreover, for the case of crater target about 100% laser absorption efficiency can be expected because of multiple laser reflections inside the crater contributing to the absorption [18]. From the above considerations we can conclude that the cylindrical crater target is a promising method to generate high flux, high energy electrons.

In the following section we introduce a combined scheme of ultraintense laser machining and laser acceleration by sequential processing with two consecutive pulses in high repetition rate and demonstrate the reproducibility of this efficient electron generation method with a simple disk target in an automatic and long (hours) operation time.

II. EXPERIMENTAL SETUP

The experiment has been performed at the Centro de Laseres Pulsados (CLPU) facility by using the Ti:sapphire 200 TW laser system VEGA-II, with a pulse width of 30 fs, 4 J of
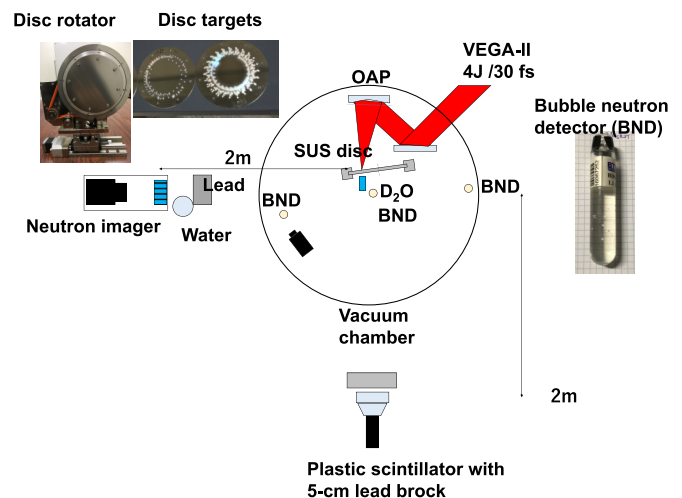

FIG. 2. Experimental setup and photos of the target and bubble detector.

energy, and capable of operating at frequency up to 10 Hz. Fig. 2 shows the experimental setup at CLPU; the 4-J VEGA-2 laser pulse was focused using an F#4 off-axis parabola on the target with 25° incident angle with a spot size of 7 μm full width at half maximum (20% encircled energy within the area) achieving a peak laser intensity of 1×10^{20} W/cm^2 [34,35]. A 10-cm-diameter, 1-mm-thick stainless-steel (SUS) disk was used as target for generation of hot electrons and x rays. The target was irradiated with a repetition rate of 1 Hz. The target surface was refreshed every two shots by rotating the target. The surface roughness was measured to be less than 5 μm, which is smaller than the Rayleigh length of the VEGA-2 laser. A glass cell, with a diameter of 10 mm and length of 20 mm, filled with D$_2$O water to be used as neutron generator was placed at 10 mm behind the target SUS disk correspondingly to the laser focal spot position. Three bubble neutron detectors filled in an air glass cell were placed around the target to measure the neutron flux: the bubble detectors were monitored by a charge-coupled device (CCD) camera during the laser shots. Hard x-ray generation was monitored by a plastic scintillator shielded by a 5-cm-thick lead block to filter out hard x ray with energy less than 1 MeV.

III. RESULTS

A. Creation of the high aspect ratio crater via ultraintense laser manufacturing

Figure 3 represents the schematic of the two-shot sequential process (a), the optical microscope image of the craters (b), the line profiles of craters created by the first pulse and the second pulse (c), and the reliability of the crater diameter created by the first pulse (d). The inner diameter of the crater is 200 ± 14 μm and the crater depth is 403 ± 11 μm. When an ultraintense laser pulse interacts on the side wall of the crater, the laser absorption efficiency significantly increases compared to flat targets given the 65°–70° incidence angle for which the surface acceleration is most efficient. We will describe the physics in detail in Sec. III.

The cylindrical crater shape is essential to the electron acceleration process. Target processing by a single laser pulse of relatively low intensity ($I \sim 10^{15}$–10^{16} W/cm^2) with
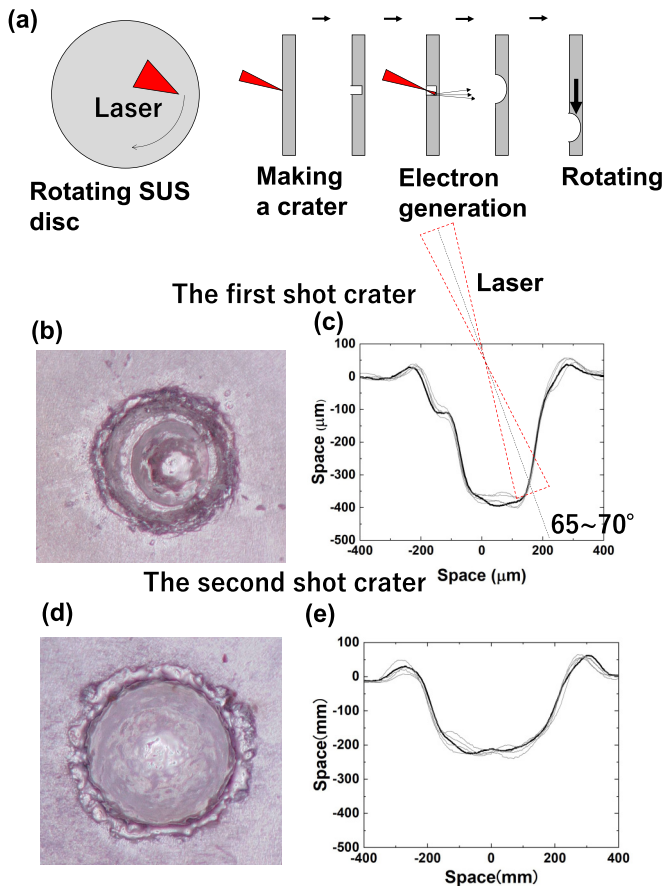
FIG. 3. (a) Schematic of the sequential pulse irradiation. (b) Microscope image of the first shot crater; note that the cylindrical section of the crater is spatially shifted compared to the spherical one as results of the directional relativistic electron beam. (d) Lineouts of craters. Five shots are plotted to indicate crater shapes are highly reproducible. (d) Microscope image of the second shot crater and (e) lineouts of craters. The second pulse is injected in the first crater and generates an ultrabright relativistic electron beam.

tight focal spot usually creates hemispherical craters. This is because the laser pulse only heats up a small portion of the target volume in a very short period, increasing the pressure and driving spherically symmetrical shock waves that ultimately determine the shape of the crater. Our peculiar crater shape is determined by nonthermal processes induced by relativistic electron beams generated by laser pulses of much higher intensity compared to the one of femtosecond laser-machining techniques. We remark that material processing by ultrahigh intensity femtosecond pulses has not been investigated. We investigated how the steep and deep cylindrical-shaped crater was created by using three simulation codes: collisional two-dimensional particle-in-cell code PICLS-2D [36], two-dimensional hydrodynamic code PINOCO-2D [37], and Monte Carlo code PHITS [38]. The electron energy density and induced ionization by laser-plasma interaction were obtained from PICLS-2D simulations. These quantities were then implemented as initial conditions into PINOCO-2D, which calculated the hydrodynamics of crater formation. The hydro code, however, is capable to simulate the thermal hydrodynamic expansion of the plasma but it cannot

simulate the nonthermal processes related to the relativistic electron ballistic transport into the target material. Therefore, the recorded relativistic electron source from the PIC code was set as input in the Monte Carlo code PHITS to calculate the deposited energy deeper into the target material.

Figure 4 represents the results for the set of simulations performed. Figure 4(a) shows the hot electron energy density calculated by PICLS-2D code, which clearly shows the heated region area corresponding to the highest electron energy density as well as the ultrarelativistic electrons propagating ballistically inside the target material. Figure 4(b) shows the hydrodynamic simulation results with the formation of circular crater as the result of hydrodynamic expansion of the heated material volume. Figure 4(c) shows the ballistic electron trajectories calculated by the Monte Carlo code PHITS and the resulting hot electron flux exceeding 10^{14} electrons/cm^2 is lined out and superposed to the experimentally measured crater profile in Fig. 4(d). This is under the assumption that the obtained crater shape is produced as a direct result of the high flux relativistic electron transport in the material. In Fig. 4(d) the simulated crater shape was magnified by an arbitrary factor 1.7 before being matched to the experimental result.

In the Monte Carlo simulation (cylindrical crater), we assumed that 10^{14} e/cm^3 is the relativistic electron density threshold for material ablation (spallation). This threshold is chosen arbitrarily since no related study has been done for high intensity lasers. The choice of this threshold does not affect the shape of crater.

We identify two different mechanisms for the creation of the crater shape: the circular (hemispherical) section of the crater is produced by thermal expansion while the deep cylindrical feature is the result of material spallation by the relativistic electron beam.

Therefore, through our analysis we can qualitatively explain the formation of this peculiar crater structure that is crucial to the brilliance and energy enhancement of the relativistic electron beam.

B. Experimental result of electron acceleration

In order to diagnose the relativistic electron-beam generation, we set up a suite of hard-x-ray and neutron diagnostics which provide indirect, yet very reliable information on the electron acceleration efficiency and electron-beam energy. In this experimental setup the SUS disk is extremely thick (1 mm) compared to standard target thicknesses in laser-plasma interaction experiments. Therefore, most of the electrons are stopped within the SUS volume, making the direct measurement of hot electron spectra via classic magnetic spectrometers unfeasible in the experiment (an electron spectrometer was equipped in the experiment but little to no electrons were recorded). Relativistic electrons were measured indirectly by their by-products consisting of hard x rays and neutrons. The hard x rays are generated by the fast electrons via bremsstrahlung emission radiated during the hot electron transport in the dense target medium. Therefore, the relativistic electron spectrum can be indirectly estimated by measuring the hard x-ray spectrum. The scintillator detector shielded by a 5-cm lead block provides a lower energy detection threshold of 1 MeV. The neutron is

(a)

2D PIC simulation
Electron energy density

Heated region **Ballistic electron**

(b)

2D hydro simulation
Density

(c) **Monte Calro simulation**
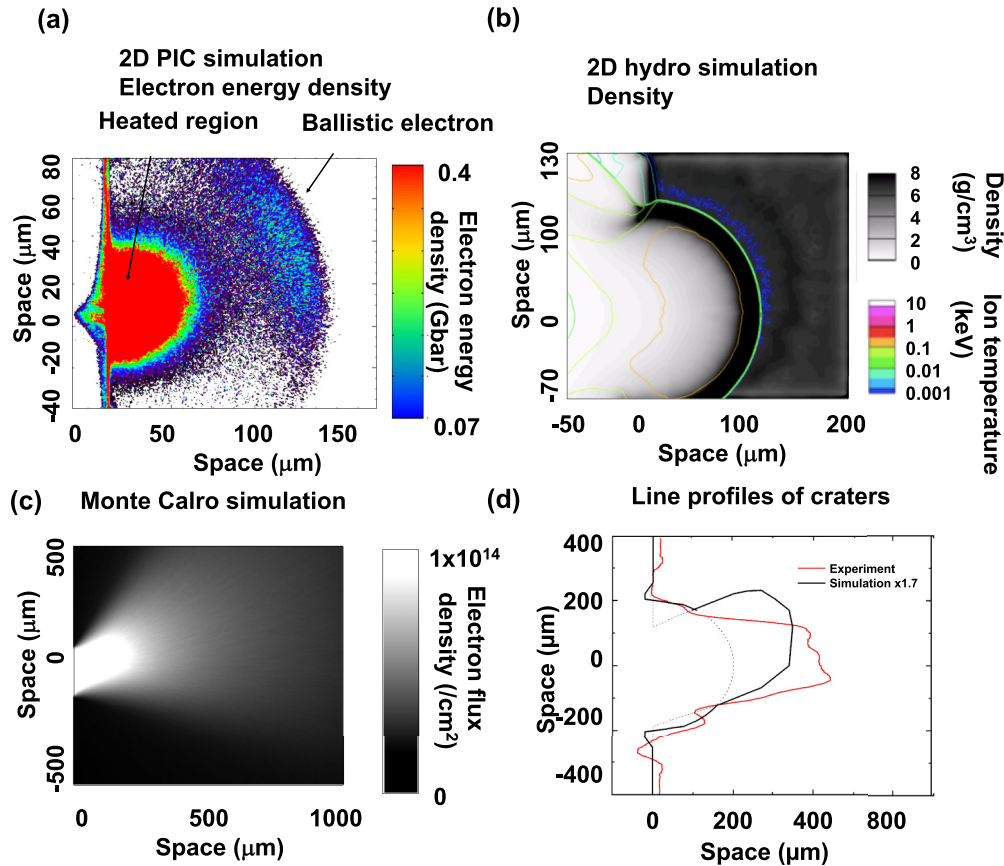
(d) **Line profiles of craters**

FIG. 4. Simulation results for crater formation. (a) Electron energy density obtained from 2D PIC simulation; (b) density and temperature map obtained by hydrodynamic simulation; (c) fast electron flux as obtained from Monte Carlo calculation. (d) Comparison of cross section of simulated (isodensity profiles in (b) and $>10^{14}/\text{cm}^3$ electron flux profile in (c) are plotted in (d) after being multiplied by 1.7 scaling factor) and experimentally observed crater clearly showing that the simulation results can qualitatively reproduce our experiment.

generated via photonuclear reaction between the hard x rays and the deuterons with a steplike cross-section function that allows neutron generation for x-ray energies >2.2 MeV [see Fig. 7(b)]. From these measurements we can estimate the hot electron spectrum via Monte Carlo simulations.

The hard x-ray diagnostic consisted of a plastic scintillator shielded by a 5-cm lead block to discriminate for x rays with energies higher than 1 MeV. Example data for this diagnostic are shown in Fig. 5, where the integral of oscilloscope waveform for the first shot (red line) and the second shot (black line) were, respectively, $(330 \pm 2)10^{-9}$ Vs (or 6.6 nC) and $(1380 \pm 8)10^{-9}$ Vs (27.6 nC). Therefore, we have a 4.2 times enhancement in hard x-ray yield with the two-shot sequential approach. We also tested the hard x-ray yield for a third sequential shot and the x-ray signal reduced to the level of single-shot irradiation. This is due to the crater geometry that, after the second shot, becomes round shaped and shallower compared to the one after the first shot [see Fig. 3(c)].

We would like to remark that although we only represented one image of oscilloscope traces from the plastic scintillator, the results were consistently obtained over more than 100 shots with great reliability.

Neutron diagnostics were constituted by bubble detectors and a neutron-imaging detector. In our experiment neutrons are created by hard x-ray-deuterium photonuclear reaction, provided by the D_2O glass cell described in the previous

section of the paper. After 150 consequent shots, 14 neutron counts in the bubble detector were detected. The bubble detector used in the experiment was BDS 600 sensitive to neutrons with energies from 0.5 to 10 MeV. The neutron yield at the target for this energy range was estimated to be $(1.7 \pm 0.7) \times 10^7$ (for 4π solid angle) per sequential shots, with the assumption of isotropic neutron emission. The 150
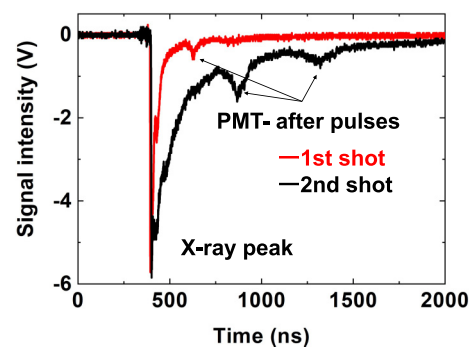
FIG. 5. Example of scintillator oscilloscope signals. The red curve corresponds to a single pulse irradiation and the black curve corresponds to the second pulse interacting with the crater wall. The hard x-ray signal is 4.2 times higher than for simple irradiation of a flat target.

(a)

(b)

(c) X-ray image

X-flux = 10^6 x/cm^2

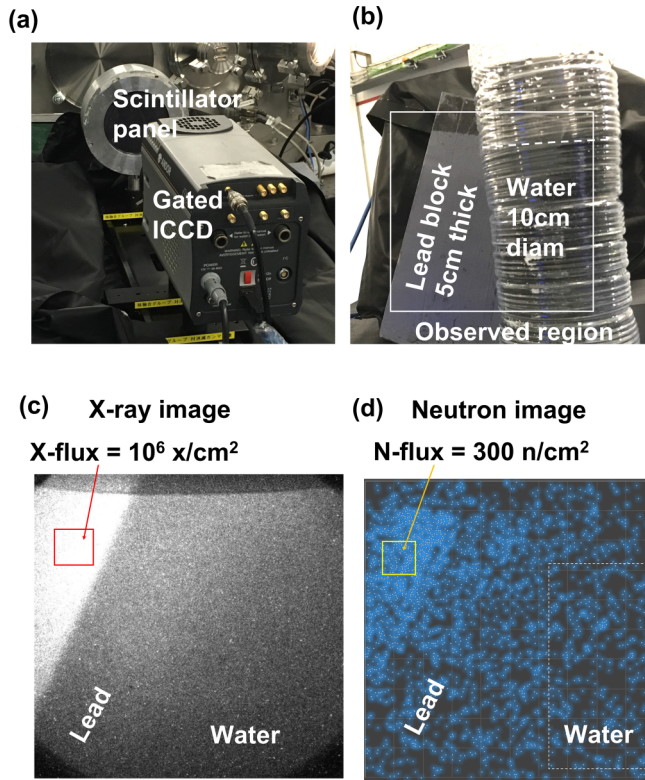**(d) Neutron image**

N-flux = 300 n/cm^2

FIG. 6. (a) Photo of neutron flux monitor; (b) lead and water were placed in front of the scintillator panel; (c) x-ray image and neutron image.

sequential shots generated a total of $(2.6 \pm 1.1) \times 10^9$ neutrons in the energy range 0.5 to 10 MeV. The neutron yield for nonsequential shots (target surface was refreshed for each shot) was $(3.5 \pm 2.7) \times 10^3$ per shot. We therefore observed 4800 times neutron yield enhancement for two sequential shots, providing further confirmation of the effectiveness of this technique in generating bright ultrarelativistic electron beams.

The neutron flux was also monitored by neutron-imaging detector to cross check the neutron flux obtained by the bubble detector. Figure 6 shows (a) photo of the detector while (b) and (c) show, respectively, a lead brick and a water bottle that were placed in front of the scintillation panel and the related hard x ray and neutron radiographs. The imaging detector consists of a liquid scintillator-based pixeled scintillator array panel and gated-image intensifier CCD [39]. F-number 0.95 imaging lens ensures a high detection efficiency so that single-count neutron signals can be discriminated. X-ray radiograph was taken by imaging a liquid scintillator by a gated 16-bit ICDD camera with 10-ns time gate centered at the time of the shot and we can clearly observe the shadow casted by the lead brick. The pixeled scintillator creates neutron-induced scintillation lights from a pixel; then, it is observed as a bright spot in the ICCD. The neutron image was taken with a time gating of 100-ns duration and by image reconstruction the bright scintillation spots, corresponding to neutron signal, were selected, and accumulated over 100 sequential shots. The neutron flux on the detector was 300 neutrons per cm^2,

corresponding to a neutron yield of 1×10^7 neutrons per shot, in agreement with the bubble detector measurement.

C. Simulation of electron generation with single- and sequential shot

In order to better understand the physics at the origin of the relativistic electron source enhancement by two-shot sequential target irradiation we performed two-dimensional PIC simulation using the code EPOCH 2D [40] followed by simulations with the Monte Carlo code PHITS [38]. The two cases of single- and two sequential shots irradiation were studied with a simplified crater target for the latter case. In the simulations we assumed a preformed plasma of 0.5-μm scale length resulting from the very high contrast ($\sim 10^{10}$) of Vega-2 laser [34,35]. In the simulation we adopted a mesh size of l/40, to resolve the laser skin depth c/ω_p with two cells. The simulation domain size is $60 \times 60 \,\mu$m for the flat target case and $100 \times 80 \,\mu$m for the crater case. Smooth currents algorithms to minimize the numerical heating and noise in the simulation have been applied, together with smoothed iterations, stride filtering, and current smoothing during the particle push. These tools prevent numerical heating while allowing for (relatively) fast execution of the simulation. Laser energy absorption processes for ultraintense laser-plasma interaction are collisionless, especially regarding the hot electron generation mechanisms.

We therefore performed collsionless simulations on fully ionized plasma since the main goal of the simulation is to explain the fast electron generation mechanism for the two cases.

For the single-shot case, laser pulse equivalent to the tightly focused Vega-2 pulse was focused onto a flat surface with an incidence angle of 20°, while for the two sequential shots case, the laser pulse was focused onto the crater wall with an incidence angle of 70° as shown in Fig. 1. Spatial profiles of the laser spots were also adjusted to the experimental conditions. In the first shot, 20% of the laser energy is contained within a 7-μm focal spot with an intensity of $1 \times 10^{20} \,$W/cm^2, and the remaining 80% of energy was distributed over a larger area with less than $5 \times 10^{18} \,$W/cm^2 intensity. For the crater-case simulation instead, 100% energy was included in 30-μm focal spot diameter with an intensity of $2 \times 10^{19} \,$W/cm^2, which is the estimated laser profile considering that the best focus is about 300 μm away from the interaction region.

Snapshots of the simulation results are shown in Figs. 7(a) $\sim$ 7(d), where we represent the azimuthal component of the magnetic field together with the fast electron-energy flux whose direction and magnitude are represented by black arrows. For the single-shot case, at 20° incidence angle a significant fraction of the laser energy is reflected at the target surface owing to the sharp preformed plasma profile, resulting in limited absorption into forward-moving hot electrons. Instead, in the case of sequential shots, the grazing incidence angle of the *P*-polarized laser, together with the larger spot size, strongly enhances the laser energy absorption into hot electrons via the excitation of surface plasmonics along the crater wall, mechanism that was described in the introduction of this paper. Part of the hot electrons are injected inside the target and propagate almost parallel to the crater surface, while most
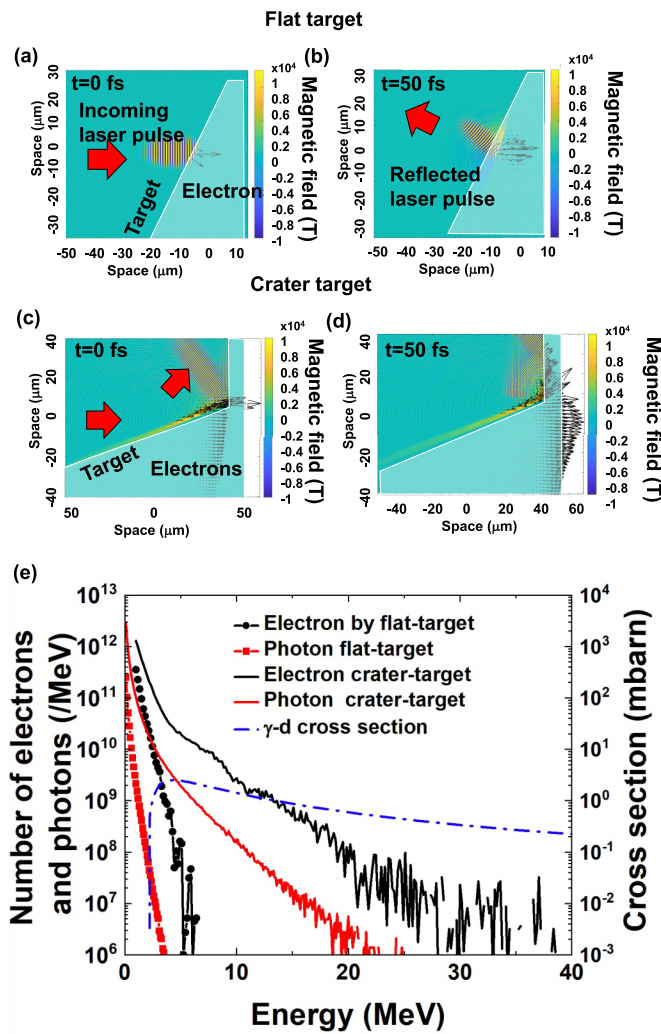
FIG. 7. (a) EPOCH2D simulation results showing the incoming laser pulse interacting with the target surface for single-shot case and (b) the laser pulse being almost completely reflected with generating a small fraction of hot electrons indicated by the black arrows (fast electron energy flux). (c) EPOCH2D simulation for the sequential-shot case. We observe a strong surface current of electrons accelerated by surface plasmonics, with a fraction of these electrons injected inside the surface and propagating alongside the laser pulse. (d) Fast electron current injected at the bottom of the crater resulting in a much brighter relativistic electron beam. The multiple reflections of the laser pulse on the crater wall and bottom cause the high laser energy absorption of 97% calculated in the simulation. (e) Fast electron energy spectra for single shot and two sequential shots represented, respectively, in black and related hard x-ray generation in red.

of the electrons accelerated by surface plasmonics are confined along the crater surface by the large ($\sim$10-kT) magnetic field and are finally injected into the highly dense plasma at the bottom of the crater. In the simulation surface plasmonics acceleration and electron accelerated normal to the target by vacuum heating and Brunel effect are both observed in the PIC simulation and all electrons are measured. The extraction planes for collection of the fast electron distribution are positioned on three sides of the simulation box. Because of very large incidence angles, even hot electrons generated by

vacuum heating and Brunel effect are also mostly directed along the surface. This is due to the formation of a large magnetic field right at the target surface, due to the large fast electron current density component that prevents large number of hot electrons from penetrating inside the target. The detailed mechanism on the process is described in Ref. [30].

Table I summaries values obtained by simulation and experiments. In the first shot, 32.5% of the laser energy is absorbed and 0.9% is converted into the fast electrons; in the second shot, 97.5% of the laser energy is absorbed and 8.2% is converted to the fast electrons. In Fig. 7(e), a comparison of the electron-energy spectra for the two cases is shown with black lines. Electron slope temperature and number are successfully increased from 0.4 to 3 MeV and from 1×10^{11} to 6.3×10^{11} per shot, respectively. These values agree very well with the theoretical estimation in Sec. I.

PHITS simulations were performed to reproduce the x-ray and neutron signals from the obtained electron spectra. Equivalent electron sources to those obtained by the EPOCH simulation were injected into the target SUS disk with a D_2O cell. It was confirmed that all neutrons were generated by the D_2O and no neutrons were generated from the SUS disk. The neutron yield for the first and the second shots are 1.5×10^3 and 2.0×10^6, respectively, with neutron generation boosted by 1300 times. Although there is a discrepancy between the experimentally observed $[(1.7 \pm 0.7) \times 10^7]$ and the simulation (2.0×10^6) in the neutron yield, the experimental data are qualitatively reproduced.

The photonuclear reaction cross section is plotted in Fig. 7(b) on the right y axis. The neutron production abruptly increases when x-ray energy exceeds 2.2 MeV, which in turn is generated by ultrarelativistic electrons with energies significantly higher than 2.2 MeV. Since the cross section of γ-d photo nuclear reaction is a steplike function at 2.22 MeV, the neutron production increases in a highly nonlinear way when the x-ray distribution significantly exceeds the 2.22-MeV threshold by the superthermal electron generation; the increment of the neutron signal is the convolution between the cross section and the x-ray spectra for the two cases.

This boosting mechanism by the double shooting realized the production of a practical neutron flux for imaging application. We concluded that the double-shooting method improved the magnitude of quantum yield on high repetition ultraintense laser accelerator. Since the method is quite simple, it can be a promising scheme for many applications in next-generation laser accelerators.

IV. CONCLUSION

In conclusion we demonstrated an efficient method to significantly increase the brilliance and energy of ultraintense laser-generated electron beams by sequential target processing using the laser pulse itself as a machining tool. This method allows for high repetition rate operation and has excellent shot-to-shot stability. In this method the first pulse created a steep cylindrical crater and the second pulse accelerated electrons from laser interaction with the crater wall via surface plasmonics mechanism. The high aspect ratio cylindrical crater shape is generated via nonthermal laser processing by the laser-generated relativistic electron beam.

TABLE I. Table summarizing the simulation and experimental results for this work.

	Flat target	Crater target	Increment factor
Laser absorption efficiency (sim)	32.5%	97.5%	3
Laser to hot electron energy (J) and conversion efficiency (sim), α	0.036 J	0.33 J	9.1
	0.9%	8.2%	
Electron temperature (sim)	0.4 MeV	T_1 : 0.3 MeV(0.98)	7.5
		T_2 : 3 MeV(0.02)	
Total electron number (sim)	1.0×10^{11}	6.3×10^{11}	6.3
Total x ray energy (sim)	0.0017 J	0.053 J	31
Neutron yield (sim)	1.5×10^3	2.0×10^6	1300
Hard x-ray signal (exp)	6.6 nC	27.6 nC	4.2
(photomultiplier tube signal)			
Neutron yield (exp)	$3.5 \pm 2.7 \times 10^3$	$1.7 \pm 0.7 \times 10^7$	4800

The dramatic enhancement in hot electrons, x rays, and neutrons was confirmed by both experiment and simulations. We believe that this method will find numerous applications in laser-plasma physics for the generation of bright electron and radiation sources.

[1] A. Nagimova and A. Perveen, A review on laser machining of hard to cut material, Mater. Today Proc. **18**, 2440 (2019).

[2] A. C. Forsman, P. S. Banks, M. D. Perry, E. M. Campbell, A. L. Dodell, and M. S. Armas, Double-pulse machining as a technique for the enhancement of material removal rates in laser machining of metals, J. Appl. Phys. **98**, 033302 (2005).

[3] M. F. Modest, Three-dimensional, transient model for laser machining of ablating/decomposing materials, Int. J. Heat Mass Transfer **39**, 221 (1996).

[4] Z. Zhao, L. Cao, L. Cao, J. Wang, W. Huang, W. Jiang, Y. He, Y. Wu, B. Zhu, K. Dong, Y. Ding, B. Zhang, Y. Gu, M. Y. Yu, and X. T. He, Acceleration and guiding of fast electrons by a nanobrush target, Phys. Plasmas **17**, 123108 (2010).

[5] T. Tajima, Laser acceleration and its future, Proc. Jan Acad. Ser. B Phys. Biol. Sci. **86**, 147 (2010).

[6] A. E. Hussein, A. V. Arefiev, T. Batson, H. Chen, R. S. Craxton, A. S. Davies, D. H. Froula, Z. Gong, D. Haberberger, Y. Ma, P. M. Nilson, W. Theobald, T. Wang, K. Weichman, G. J. Williams, and L. Willingale, Towards the optimisation of direct laser acceleration, New J. Phys. **23**, 023031 (2021).

[7] C. Gahn, G. D. Tsakiris, A. Pukhov, J. Meyer-Ter-Vehn, G. Pretzler, P. Thirolf, D. Habs, and K. J. Witte, Multi-MeV Electron Beam Generation by Direct Laser Acceleration in High-Density Plasma Channels, Phys. Rev. Lett. **83**, 4772 (1999).

[8] R. Cauble, L. B. Da Silva, T. W. Barbee, P. Celliers, J. C. Moreno, and A. S. Wan, Micron-Resolution Radiography of Laser-Accelerated and X-Ray Heated Foils with an X-Ray Laser, Phys, Rev. Lett. **74**, 3816 (1995).

[9] S. Fritzler, V. Malka, G. Grillon, J. P. Rousseau, F. Burgy, E. Lefebvre, E. D'Humières, P. McKenna, and K. W. D. Ledingham, Proton beams generated with high-intensity lasers: Applications to medical isotope production, Appl. Phys. Lett. **83**, 3039 (2003).

[10] A. Yogo, S. R. Mirfayzi, Y. Arikawa, Y. Abe, T. Wei, T. Mori, Z. Lan, Y. Hoonoki, D. O. Golovin, K. Koga, Y. Suzuki, M. Kanasaki, S. Fujioka, M. Nakai, T. Hayakawa, K. Mima, H. Nishimura, S. Kar, and R. Kodama, Single shot radiography by a bright source of laser-driven thermal neutrons and x-rays, Appl. Phys. Express **14**, 106001 (2021).

[11] S. R. Mirfayzi, A. Yogo, Z. Lan, T. Ishimoto, A. Iwamoto, M. Nagata, M. Nakai, Y. Arikawa, Y. Abe, D. Golovin, Y. Honoki, T. Mori, K. Okamoto, S. Shokita, D. Neely, S. Fujioka, K. Mima, H. Nishimura, S. Kar, and R. Kodama, Proof-of-principle experiment for laser-driven cold neutron source, Sci. Rep. **10**, 1 (2020).

[12] T. Mori, A. Yogo, T. Hayakawa, S. R. Mirfayzi, Z. Lan, Y. Abe, Y. Arikawa, D. Golovin, T. Wei, Y. Honoki, M. Nakai, K. Mima, H. Nishimura, S. Fujioka, and R. Kodama, Direct evaluation of high neutron density environment using (n, 2n) reaction induced by laser-driven neutron source, Phys. Rev. C **104**, 015808 (2021).

[13] Z. Lan and A. Yogo, Exploring nuclear photonics with a laser driven neutron source, Plasma Phys. Control. Fusion **64**, 024001 (2022).

[14] S. C. Wilks, S. C. Wilks, W. L. Kruer, M. Tabak, and A. B. Langdon, Absorption of Ultra-Intense Laser Pulses, Phys. Rev. Lett. **69**, 1383 (1992).

[15] Erik Lefebvre and Guy Bonnaud, Nonlinear electron heating in ultrahigh-intensity-laser–plasma interaction, Phys. Rev. E **55**, 1011 (1997).

[16] M. Zimmer, S. Scheuren, A. Kleinschmidt, N. Mitura, A. Tebartz, G. Schaumann, T. Abel, T. Ebert, M. Hesse, Ş. Zähter, S. C. Vogel, O. Merle, R.-J. Ahlers, S. Duarte Pinto, M. Peschke, T. Kröll, V. Bagnoud, C. Rödel, and M. Roth, Demonstration of non-destructive and isotope-sensitive material analysis using a short-pulsed laser-driven epi-thermal neutron source, Nat. Commun. **13**, 1173 (2022).

[17] I. Prencipe, J. Fuchs, S. Pascarelli, D. W. Schumacher, R. B. Stephens, N. B. Alexander, R. Briggs, M. Büscher, M. O. Cernaianu, A. Choukourov, M. De Marco, A. Erbe, J. Fassbender, G. Fiquet, P. Fitzsimmons, C. Gheorghiu, J. Hund, L. G. Huang, M. Harmand, N. J. Hartley, A. Irman, T. Kluge, Z. Konopkova, S. Kraft, D. Kraus, V. Leca, D. Margarone, J. Metzkes, K. Nagai, W. Nazarov, P. Lutoslawski, D. Papp, M. Passoni, A. Pelka, J. P. Perin, J. Schulz, M. Smid, C. Spindloe, S. Steinke, R. Torchio, C. Vass, T. Wiste, R. Zaffino, K. Zeil, T. Tschentscher, U. Schramm, and T. E. Cowan, Targets for high repetition rate laser facilities: Needs, challenges and perspectives, High Power Laser Sci. Eng. **5**, 17 (2017).

[18] T. Nakamura, H. Sakagami, T. Johzaki, H. Nagatomo, and K. Mima, Generation and transport of fast electrons inside cone targets irradiated by intense laser pulses, Laser Part. Beams **24**, 5 (2006).

[19] T. Ma, H. Sawada, P. K. Patel, C. D. Chen, L. Divol, D. P. Higginson, A. J. Kemp, M. H. Key, D. J. Larson, S. Le Pape, A. Link, A. G. Macphee, H. S. Mclean, Y. Ping, R. B. Stephens, S. C. Wilks, and F. N. Beg, Hot Electron Temperature and Coupling Efficiency Scaling with Prepulse for Cone-Guided Fast Ignition, Phys. Rev. Lett. **108**, 115004 (2012).

[20] S. Vallières, M. Salvadori, A. Permogorov, G. Cantono, K. Svendsen, Z. Chen, S. Sun, F. Consoli, E. d'Humières, C.-G. Wahlström, and P. Antici, Enhanced laser-driven proton acceleration using nanowire targets, Sci. Rep. **11**, 2226 (2021).

[21] M. M. Günther, O. N. Rosmej, P. Tavana, M. Gyrdymov, A. Skobliakov, A. Kantsyrev, S. Zähter, N. G. Borisenko, A. Pukhov, and N. E. Andreev, Forward-looking insights in laser-generated ultra-intense γ-ray and neutron sources for nuclear application and science, Nat. Commun. **13**, 170 (2022).

[22] S. C. Wilks, A. B. Langdon, T. E. Cowan, M. Roth, M. Singh, S. Hatchett, M. H. Key, D. Pennington, A. MacKinnon, and R. A. Snavely, Energetic proton generation in ultra-intense laser-solid interactions, Phys. Plasmas **8**, 542 (2001).

[23] B. Chrisman, Y. Sentoku, and A. J. Kemp, Intensity scaling of hot electron energy coupling, Phys. Plasmas **15**, 056309 (2008).

[24] L. Chopineau, A. Leblanc, G. Blaclard, A. Denoeud, M. Thévenet, J. L. Vay, G. Bonnaud, P. Martin, H. Vincenti, and F. Quéré, Identification of Coupling Mechanisms between Ultraintense Laser Light and Dense Plasmas, Phys. Rev. X **9**, 011050 (2019).

[25] A. V. Arefiev, B. N. Breizman, M. Schollmeier, and V. N. Khudik, Parametric Amplification of Laser-Driven Electron Acceleration in Underdense Plasma, Phys. Rev. Lett. **108**, 145004 (2012).

[26] Y. Takahashi, Y. Kiyanagi, K. Watanabe, A. Uritani, T. Sano, J. Hori, and K. Nakajima, Development of a neutron source for imaging at the electron linac facility in Kyoto University Research Reactor Institute, Physica B **551**, 488 (2018).

[27] E. Esarey, C. B. Schroeder, and W. P. Leemans, Physics of laser-driven plasma-based electron accelerators, Rev. Mod. Phys. **81**, 1229 (2009).

[28] F. Salehi, M. Le, L. Railing, M. Kolesik, and H. M. Milchberg, Laser-Accelerated, Low-Divergence 15-MeV Quasimonoenergetic Electron Bunches at 1 KHz, Phys. Rev. X **11**, 021055 (2021).

[29] T. Tajima and J. M. Dawson, Laser Electron Accelerator, Phys. Rev. Lett. **43**, 267 (1979).

[30] T. Nakamura, S. Kato, H. Nagatomo, and K. Mima, Surface-Magnetic-Field and Fast-Electron Current-Layer Formation by Ultraintense Laser Irradiation, Phys. Rev. Lett. **93**, 265002 (2004).

[31] T. Nakamura, K. Mima, H. Sakagami, and T. Johzaki, Electron surface acceleration on a solid capillary target inner wall irradiated with ultraintense laser pulses, Phys. Plasmas **14**, 053112 (2007).

[32] L. Fedeli, A. Sgattoni, G. Cantono, D. Garzella, F. Réau, I. Prencipe, M. Passoni, M. Raynaud, M. Kv, J. Proska, A. Macchi, and T. Ceccotti, Electron Acceleration by Relativistic Surface Plasmons in Laser-Grating Interaction, Phys. Rev. Lett. **116**, 015001 (2016).

[33] M. Raynaud, J. Kupersztych, C. Riconda, J. C. Adam, and A. Héron, Strongly enhanced laser absorption and electron acceleration via resonant excitation of surface plasma waves, Phys. Plasmas **14**, 092702 (2007).

[34] M. Huault, G. Zeraouli, J. G. Ajates, J. Apiñaniz, E. García, I. Hernández, S. Malko, C. Méndez, J. A. Perez, J. D. Pisonero, C. Salgado, X. Vaisseau, O. Varela, G. Gatti, L. Volpe, L. Roso, R. Fedosejevs, A. Longman, R. Shepherd, and W. T. Hill, Commissioning experiments of VEGA-2 at Centro de Láseres Pulsados (CLPU), in *Frontiers in Optics, 2017, OSA Technical Digest (online)* (Optica Publishing Group, 2017).

[35] L. Volpe, R. Fedosejevs, G. Gatti, J. A. Pérez-Hernández, C. Méndez, J. Apiñaniz, X. Vaisseau, C. Salgado, M. Huault, S. Malko, G. Zeraouli, V. Ospina, A. Longman, D. De Luis, K. Li, O. Varela, E. García, I. Hernández, J. D. Pisonero, J. García Ajates, J. M. Alvarez, C. García, M. Rico, D. Arana, J. Hernández-Toro, and L. Roso, Generation of high energy laser-driven electron and proton sources with the 200 TW System VEGA 2 at the Centro de Laseres Pulsados, High Power Laser Sci. Eng. **7**, e25 (2019).

[36] Y. Sentoku and A. J. Kemp, Numerical methods for particle simulations at extreme densities and temperatures: Weighted particles, relativistic collisions and reduced currents, J. Comput. Phys. **227**, 6846 (2008).

[37] H. Nagatomo, T. Johzaki, T. Nakamura, H. Sakagami, and K. Mima, Computational studies and designs for fast ignition, AIP Conf. Proc. **876**, 361 (2006).

[38] T. Sato, Y. Iwamoto, S. Hashimoto, T. Ogawa, T. Furuta, S. Ichiro Abe, T. Kai, P. E. Tsai, N. Matsuda, H. Iwase, N. Shigyo, L. Sihver, and K. Niita, Features of Particle and Heavy Ion Transport Code System (PHITS) Version 3.02, J. Nucl. Sci. Technol. **55**, 684 (2018).

[39] Y. Arikawa, S. Matsubara, Y. Abe, Y. Kato, H. Kishimoto, A. Yogo, H. Nishimura, M. Nakai, H. Shiraga, S. Fujioka,

H. Azechi, Y. Otake, K. Mima, and Y. Honda, Large aperture fast neutron imaging detector with 10-ns time resolution, SPIE Proceedings, Selected Papers from the 31st International Congress on High-Speed Imaging and Photonics **10328**, 103280T (2017).

[40] T. D. Arber, K. Bennett, C. S. Brady, A. Lawrence-Douglas, M. G. Ramsay, N. J. Sircombe, P. Gillies, R. G. Evans, H. Schmitz, A. R. Bell, and C. P. Ridgers, Contemporary particle-in-cell approach to laser-plasma modelling, Plasma Phys. Controlled Fusion **57**, 113001 (2015).